

Title: Leveraging the Human Ventral Visual Stream to Improve Neural Network Robustness

Authors: Zhenan Shao^{1,2,3,†,*}, Linjian Ma^{3,†}, Bo Li^{3,4}, Diane M. Beck^{1,2}

Affiliations:

¹Department of Psychology, University of Illinois Urbana-Champaign

²The Beckman Institute, University of Illinois Urbana-Champaign

³Department of Computer Science, University of Illinois Urbana-Champaign

⁴Department of Computer Science, University of Chicago

*Correspondence: zhenans2@illinois.edu

†These authors contributed equally to this work

Abstract:

Human object recognition exhibits remarkable resilience in cluttered and dynamic visual environments¹⁻⁵. In contrast, despite their unparalleled performance across numerous visual tasks⁶, Deep Neural Networks (DNNs) remain far less robust than humans⁷, showing, for example, a surprising susceptibility to adversarial attacks involving image perturbations that are (almost) imperceptible to humans⁸. Human object recognition likely owes its robustness, in part, to the increasingly resilient representations that emerge along the hierarchy of the ventral visual cortex⁹. Here we show that DNNs, when guided by neural representations from a hierarchical sequence of regions in the human ventral visual stream, display increasing robustness to adversarial attacks. These neural-guided models also exhibit a gradual shift towards more human-like decision-making patterns and develop hierarchically smoother decision surfaces. Importantly, the resulting representational spaces differ in important ways from those produced by conventional smoothing methods, suggesting that such neural-guidance may provide previously unexplored robustness solutions. Our findings support the gradual emergence of human robustness along the ventral visual hierarchy and suggest that the key to DNN robustness may lie in increasing emulation of the human brain.

Main Text

Humans demonstrate remarkable proficiency in visual processing, seamlessly navigating through the complex and dynamic visual environment. Empirical evidence has consistently demonstrated our ability to recognize objects despite changes in translation¹, scale³, viewpoints², and evolutionarily unnatural image degradations⁴ for even novel, and therefore untrained, objects⁵. Interestingly, DNNs, despite unparalleled performance on visual tasks⁶ and inspirations drawn from biological architectures¹⁰, fail many of the invariance benchmarks that humans excel at^{4,7,11–13}.

The lack of robustness of current artificial intelligence (AI) applications is understandably an area of great concern in computer vision, especially in the consequential areas of autonomous driving and medical diagnosis. Adversarial attacks, that is, carefully crafted image perturbations designed to deceive a model, pose a significant challenge to the robustness of the DNNs¹⁴. A particularly important class of adversarial attacks are those that generate image perturbations (almost) imperceptible and therefore innocuous to humans⁸, but can nonetheless reduce DNNs' performance to chance (See one example in Fig. 2a).

Such stark contrasts between the robust human visual system and the brittle DNNs could be a result of them learning to build importantly different representations. Empirical studies^{15,16}, along with computational models¹⁷ and theoretical frameworks⁹ suggested a significant role for the ventral visual stream of the brain, encompassing visual cortices such as V1, V2, and hV4, through to the inferotemporal (IT) cortex, in object representation. In particular, as visual inputs traverse these hierarchically organized regions, their representation becomes increasingly stable as a result of increasingly disentangled representation spaces⁹. In other words, visual inputs belonging to the same object category become increasingly tolerant to identity-preserving transformations and more separable from nearby categories by a simple linear decision hyperplane. Indeed, empirical studies^{15,18–20} that examined neural encoding patterns to various transformations of visual objects revealed a tendency towards greater stability or consistency in object representations at higher levels of the ventral stream.

Translating the principles underlying human visual robustness into DNN architectural implementations presents a significant challenge, given the current speculative understanding of the exact transformation mechanisms used within the ventral visual stream. However, if the key is indeed the evolving neural representation space, and DNNs simply lack similar “hardware” to naturally reach such a superior representation space in their later layers, then a viable approach would be to directly guide the DNNs with the representation space used by humans and see if they can achieve better resilience. More importantly, if the evolving representation space is indeed an inherent property of the ventral visual stream that gradually builds resilience, we should then expect a gradient of robustness improvement in DNNs with guidance from hierarchically later brain regions yielding more substantial gains.

Here, we used a “neural-guidance” approach^{21–23} that trains DNN models to concurrently learn visual recognition tasks and the neural representations corresponding to specific images. In particular, we trained distinct DNNs, each tuned to the neural responses from consecutive stages within the ventral visual stream. Human neural responses were obtained from the Natural Scene Dataset (NSD)²⁴ which provides whole-brain neural activity data recorded using high-resolution 7T functional Magnetic Resonance Imaging (fMRI) as human participants viewed an extensive collection of natural images. As illustrated in Fig. 1a, our approach involved training a ResNet18-based DNN on two concurrent tasks: a visual recognition task involving image classification, and a representation learning task. The latter was facilitated by an additional neural head, guiding the DNNs to align their internal representations with those derived from neural responses.

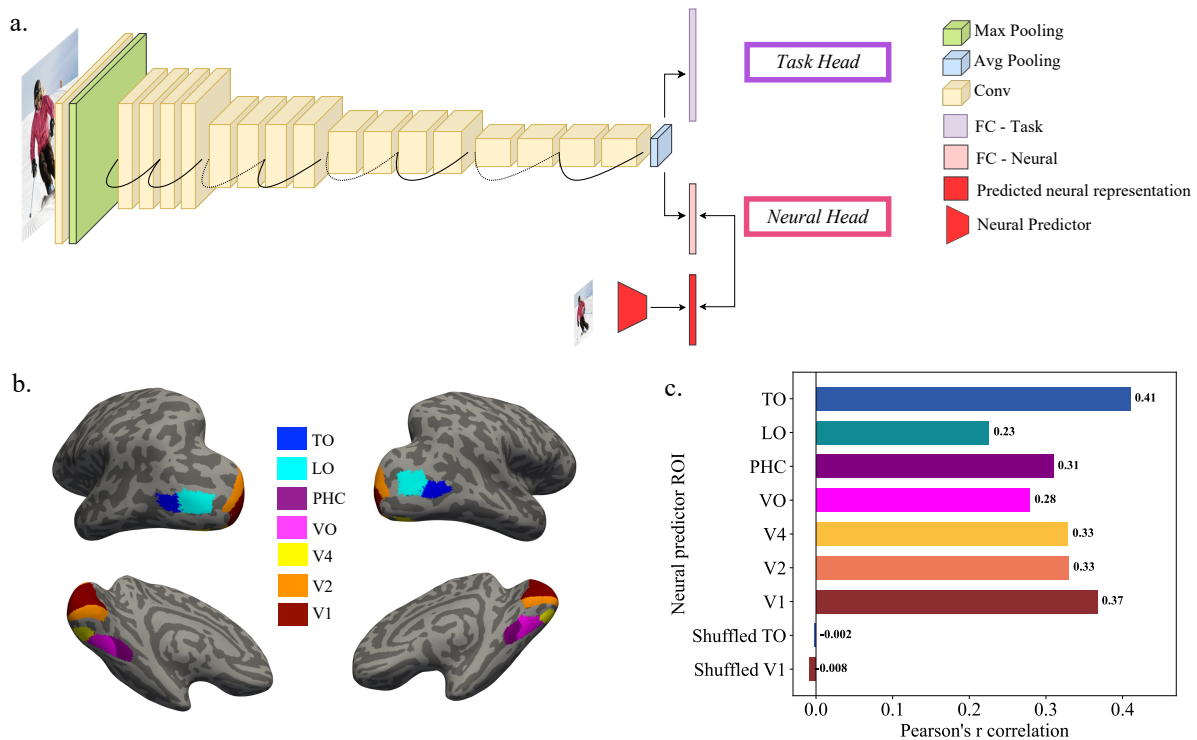


Fig 1. Schematic illustration of the neural-guidance training process. **a.** The architecture of the neurally-guided ResNet18 structure with a task head learning the primary visual recognition task, and a neural head learning the neural representation of the corresponding input images. The neural representations are generated by neural predictors, acting as surrogates for human brain regions to produce predicted neural responses (see the “neural predictors” section in Methods). **b.** Illustration of the anatomical locations of the seven Regions of Interest (ROI), V1, V2, V4, VO, PHC, LO, and TO of Subject-1²⁴. Neural responses obtained from each were used in the current experiment to guide DNNs. **c.** Quality check of the neural predictors, shown as Pearson’s r correlation between the predicted neural responses and the actual human recordings. The “Shuffled TO” and “Shuffled V1” predictors, in which the match between input images and ground-truth neural responses was intentionally permuted during the training of neural predictors, served as baseline conditions. The near-zero correlations in these shuffled conditions confirm that the higher predictability of the actual neural predictors reflects meaningful neural information related to the input images.

Neural Predictors

Given the extensive images required for DNN training and the subsequent necessity to assess the effect of neural-guidance across diverse image sets and tasks, we used the more limited neural data acquired from humans in NSD to create neural predictors (see the “neural predictors” section in Methods for details). These neural predictors served as surrogates for each brain region, providing the approximated neural responses for the extensive and diverse image sets not seen by human participants but required for the neurally-guided training.

Distinct neural predictors were trained to emulate the neural responses of each Region of Interest (ROI) along the ventral visual stream based on an anatomical atlas for the human visual cortex²⁵. Our focus spanned from the primary visual cortex V1 to V2, V4, VO (Ventral-Occipital), PHC (posterior Parahippocampal Cortex), LO (Lateral-Occipital), and TO (Temporal-Occipital) regions (illustrated in Fig. 1b) along the ventrolateral surface of the brain. V1 and V2 are retinotopically organized areas known for processing low-level details²⁶ and represent the initial stages of the cortical processing hierarchy. V4 serves as an intermediate stage. While not yet exhibiting a pronounced preference for objects, V4 demonstrates early signs of invariance¹⁵. Further along the ventral cortex lie VO and PHC. VO is positioned immediately anterior to V4 with a demonstrated object preference²⁷, while PHC, located further anterior and overlapping with the Parahippocampal Place Area (PPA) starts to show preference for scenes²⁸, indicative of its capability to extract global information. LO on the lateral surface, which includes LO1 and LO2, overlaps with the relatively posterior section of the functionally defined Lateral Occipital Complex (LOC)²⁹, commonly recognized for its holistic shape processing capabilities³⁰. Finally, TO, although less frequently investigated on its own in relation to object recognition, is situated anterior to LO, and potentially encompasses the more anterior portion of LOC²⁹.

The neural predictors’ predictive power was evaluated by Pearson’s r correlation between the predicted and actual neural patterns from each ROI, as demonstrated in Fig. 1c. We also trained predictors with shuffled V1 and TO data, where the associations between images and their ground truth neural responses were randomly permuted, serving as baseline predictors against which we can compare the quality of the ROI neural predictors. All seven ROI predictors

produced Pearson’s r correlations well above the near-zero prediction performance of the shuffled baseline predictors, confirming the utility of the neural predictors.

Hierarchical improvement in DNN robustness

The seven fully trained and frozen neural predictors were then used to generate neural representations to each guide one of seven DNNs when learning an image classification task on ImageNet images. In addition to the seven neurally-guided DNNs, we also included four baseline models each allowing us to rule out different alternative hypotheses. The “None” model, serving as the fundamental baseline, was devoid of the neural head and focused solely on the classification task. The “Random” model was guided by an untrained neural predictor with only randomly initialized weights, allowing us to rule out the possibility that the mere addition of the neural head, and therefore the associated loss term, might inadvertently lead to robustness improvement. Furthermore, we included “V1-shuffle” and “TO-shuffle” models that were guided by properly trained neural predictors, that is, the same predictors used for V1- and TO-guided DNNs. However, during training, neural representations were generated from images randomly selected and different from those the DNN was classifying at the moment, thereby guiding the DNNs with incongruent neural representations. Therefore, these two baseline models ensured that any improvements in robustness were not merely the byproduct of neural-characteristic noise, but rather meaningful information encoded in the neural representations.

To assess the adversarial robustness of the neurally-guided and baseline models, we first implemented the l_∞ -based Projected Gradient Descent (PGD) attack³¹ targeting the classification head of the models (see the “Adversarial Attacks” section in Methods). We tested the models against a range of attack strengths by varying the perturbation bounds ϵ that govern the magnitude of perturbations added to the input image (see Fig. 2a for an example). If the neurally-guided models have indeed learned representation spaces that lead to more robust performance, they should collectively outperform the baseline models under adversarial attack, particularly those guided by later stages in the visual processing hierarchy. As shown in Fig. 2b, our results indeed show that baseline models exhibited similar susceptibility to attacks, whereas all neurally-guided models demonstrated not only better resilience but a hierarchy of improvement. Models guided by V1 and V2 showed comparable levels of robustness, reflecting their early positions in

the visual processing sequence. Improvements in robustness were more pronounced in the V4-guided model and were further surpassed by the LO-guided, VO-guided, and PHC-guided models, with the TO-guided model exhibiting the highest level of robustness.

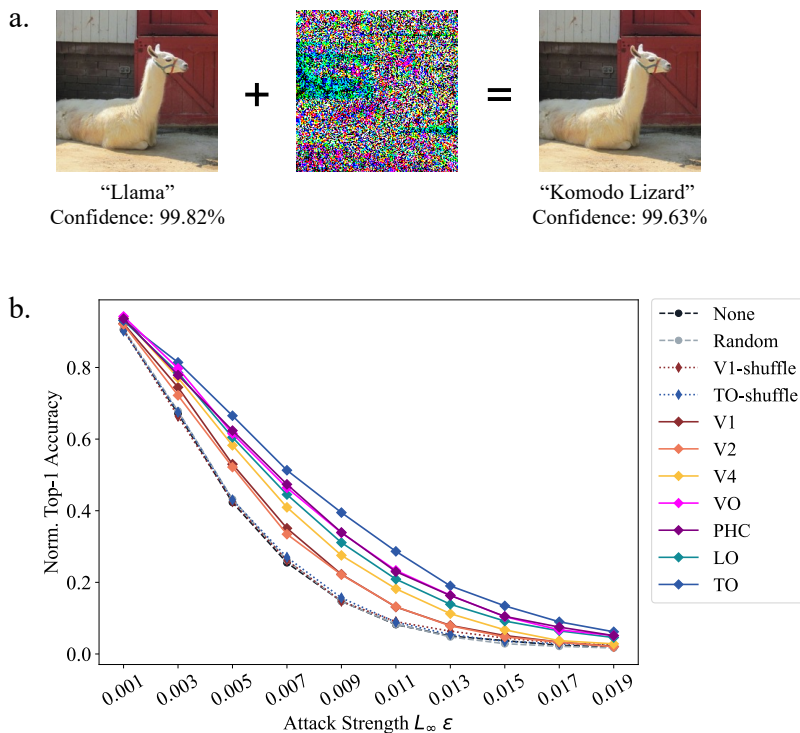


Fig 2. Neurally-guided models show hierarchical improvements in adversarial robustness.

a. An example of adversarial perturbation generated using l_∞ -based Projected Gradient Descent Attack (PGD)³¹ with an ϵ of 0.015 added to an image of a llama (obtained from the ImageNet⁶), effectively misleading the baseline “None” model to classify the perturbed image as a “Komodo lizard” with a high confidence score (99.63%). Note that the perturbed image remains visually indistinguishable from the original image. **b.** Performance of neurally-guided models and baseline models on the image classification task when subjected to the l_∞ -based PGD attack. The y-axis shows top-1 classification accuracy normalized to each model’s accuracy on unperturbed (clean) images (refer to the “Adversarial Attacks” section in Methods). Attack strength increases as ϵ increases on the x-axis.

To substantiate our observation, we further employed a variety of common adversarial attacks beyond the l_∞ -based PGD attack, including l_∞ -based Fast Gradient Sign Method (FGSM) attack³², l_∞ -based AutoAttack³³, l_2 -based FGM attack³² and l_2 -based Deepfool attack³⁴. The observed hierarchy of robustness was consistent across these additional attack methods (Supp. Fig. S1a-d), confirming that this hierarchy is not a coincidental result of one specific attack. Moreover, we extended the evaluation of our neural-guidance approach to an alternative image dataset, CIFAR-100 (Supp. Fig. S1e) using l_∞ -based PGD attack. Although the overall magnitude of robustness improvement was reduced, potentially as a result of the significantly different image statistics due to CIFAR-100's greatly reduced size, the hierarchical pattern of robustness remained evident. This replication across image datasets further confirms that the effect of neural guidance is more fundamental and not constrained to a particular dataset.

If neurally-guide models achieve better robustness indeed as a result of learning a better representation space, we would expect this improvement to extend beyond mere image classification to any task that fundamentally relies on the features extracted by the model. To explore this, we employed an image captioning task to examine whether the benefits of neural guidance persist when the model's extracted features are repurposed for a task other than classification. A common approach in image captioning involves employing a pre-trained DNN as a dedicated feature extractor, or "encoder", to process an input image, and the output is then channeled into a decoder tasked with generating image captions³⁵. We removed both heads and froze the backbone of all seven neurally-guided models and the four baseline models to preserve the feature extraction capabilities. Decoders were subsequently trained to generate captions for a collection of MSCOCO images. Thus, we were able to evaluate the impact of neural guidance with both an alternative task and a different set of images. Employing the same l_∞ -based PGD attack on the captioning task, we again found the same robustness hierarchy, consistent with our previous results (Supp. Fig. S1f). Collectively, our findings not only show that aligning DNNs with human neural representation spaces through neural responses improves model robustness, consistent with observations in recent work^{21,23} but also revealed a hierarchy of robustness improvements that increases along the ventral visual stream, further confirming that the ventral stream's function includes creating an increasingly resilient representation of visual inputs.

Neural guidance leads to smoother output surfaces

A key characteristic of robust models is their association with smoother output surfaces, or more slowly changing loss landscapes with respect to the input images³⁶. Adversarial attacks exploit the irregular and complex output surfaces of models, which not only facilitates the search for adversarial examples via gradient descent but also contributes to the existence of numerous adversarial examples around each data point. Defenses against adversarial attacks sometimes rely on this insight, aiming to mechanistically smooth the model’s output surface³⁶. Importantly, an effective representation space at the model’s final stage should naturally entail a smoother output surface. This is because in such a space, semantically similar images, including those differing only by minor perturbations, should be mapped to proximate regions, or constitute continuous manifolds⁹ that are easily separable from other object manifolds in the space.

We thus would expect that if the ventral stream is creating increasingly robust representations, then a correspondingly smoother loss landscape would likely emerge among the neurally-guided models. Indeed, visualization of the output surfaces for the “None”, “V4”-guided, and “TO”-guided models depicted in Fig. 3a show an increasingly smooth landscape. To quantitatively measure this smoothness, we calculated the magnitude of the gradient norm for adversarial examples across various neighborhood sizes³⁷ (detailed in the “Analysis” section of the Methods) and show that neurally-guided models consistently have smoother output surfaces at every evaluated neighborhood radius compared to their baseline counterparts (Fig. 3b). Notably, in accordance with the adversarial robustness performance shown in Fig. 2b, models guided by hierarchically later regions manifested increasingly smoother surfaces, with the exception of V2 being slightly less smooth than V1. We note that engineering solutions to smooth functions, such as regularization methods to encourage the generalization of a model, have been around for a long time³⁸. Importantly, however, we show in subsequent analyses that using neural-guidance to impart smoothness produces fundamentally different solutions than conventional regularization methods.

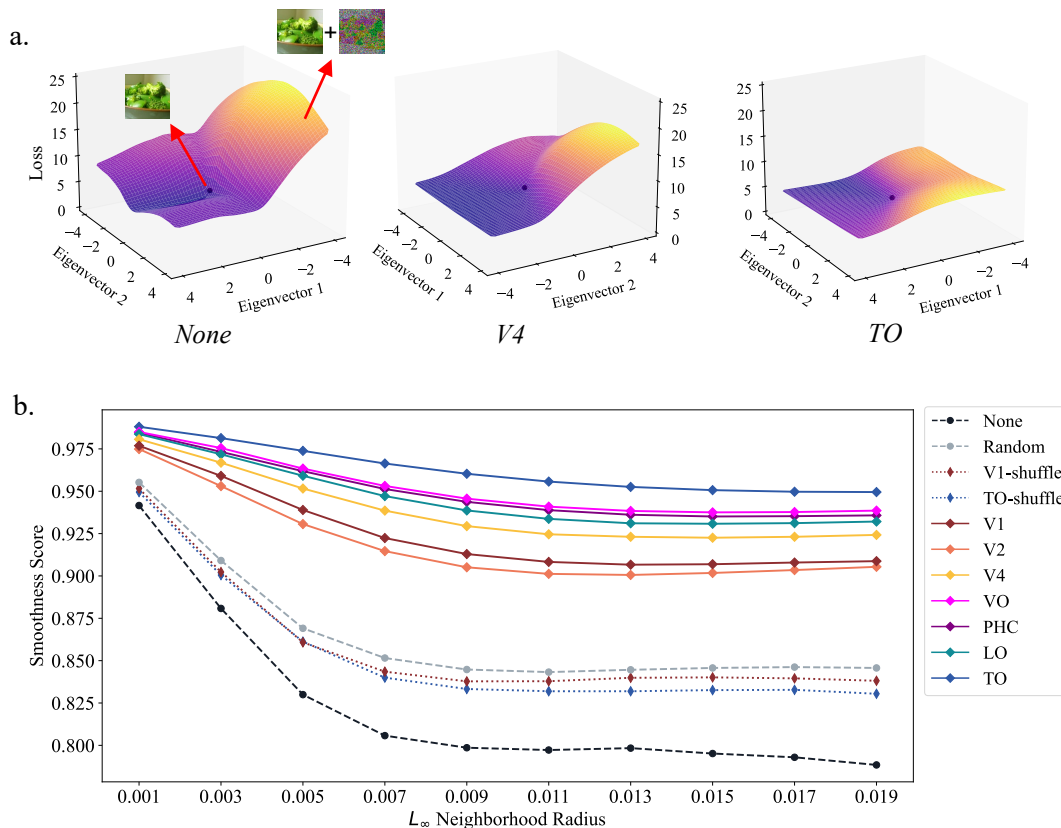


Fig 3. Neurally-guided DNNs have smoother output surfaces. **a.** Visualization of the loss landscape with respect to input images for three selected models: “None”, “V4-guided” and “TO-guided” near a reference broccoli image (obtained from the ImageNet⁶, refer to the “Analysis” section in Methods for details on surface generation). The black dot represents the unperturbed (clean) image, while other locations on the surface would denote all variants of the clean image including those found by adversarial attacks. The z-axis quantifies the task loss associated with each input image. **b.** Smoothness scores³⁷ (a.u., refer to the “Analysis” section in Methods for details) for each model, calculated within a specified l_∞ -based neighborhood radius of each clean image. Larger values correspond to smoother and more level surfaces.

Neurally-guided models are more shape-biased

We conducted several additional analyses to further distinguish neurally-guided models from standard DNNs. To allow comparison to conventional methods such as smoothness regularization, we trained five additional models, each varying in the weight decay magnitude

(WD)³⁹, to produce models with a spectrum of smoothness and robustness improvements (refer to the “Analysis” section in Methods for details, and see Supp. Fig. S2 for diagnostics on WD models). In comparison to these WD as well as baseline models, we first show that neurally-guided models develop more human-like properties, such as the shape bias.

We hypothesized that neurally-guided models should increasingly capture higher-level, global, and abstract features conducive to constructing a representation of object shapes as one ascends the ventral stream. Previous research has consistently shown that, in contrast to machines’ preference for textural cues, human visual perception almost exclusively relies on shape cues to discern objects⁴⁰. Moreover, the distortions introduced by adversarial attacks can be interpreted as subtle disturbances of image textures (as illustrated in Fig. 2a), suggesting that a model’s shift toward shape-based recognition might improve its resilience to such perturbations. Using style-transferred images⁴¹, we found that neurally-guided models, especially those guided by higher regions, indeed exhibited a higher tendency towards shape-based decision-making, along with their increased resilience against adversarial perturbations.

Style-transferred images were created by merging the texture of one object (e.g. broccoli) with the shape of another (e.g. a llama) (Illustrated in Fig. 4a). When processing these images, a model might prioritize shape (identifying the image as a llama), texture (classifying it as broccoli), or make a mistake. Our results (Fig. 4b) show that the baseline models predominantly favored texture-based decisions. However, a notable transition occurs for neurally-guided DNNs when we progress through the ventral stream, from the early visual areas V1 and V2 to the more advanced regions. More importantly, while WD models with higher weight decay values show some improvement, they do not demonstrate a comparable level of shape bias, particularly when compared against hierarchically later regions. Neurally-guided models’ steady shift towards shape-based decisions supports the evolving abstraction capabilities inherent in the ventral visual stream, potentially underpinning its robustness. Similar properties, on the other hand, were not fostered in models trained with smoothness regularization alone, despite them exhibiting comparable levels of output surface smoothness.

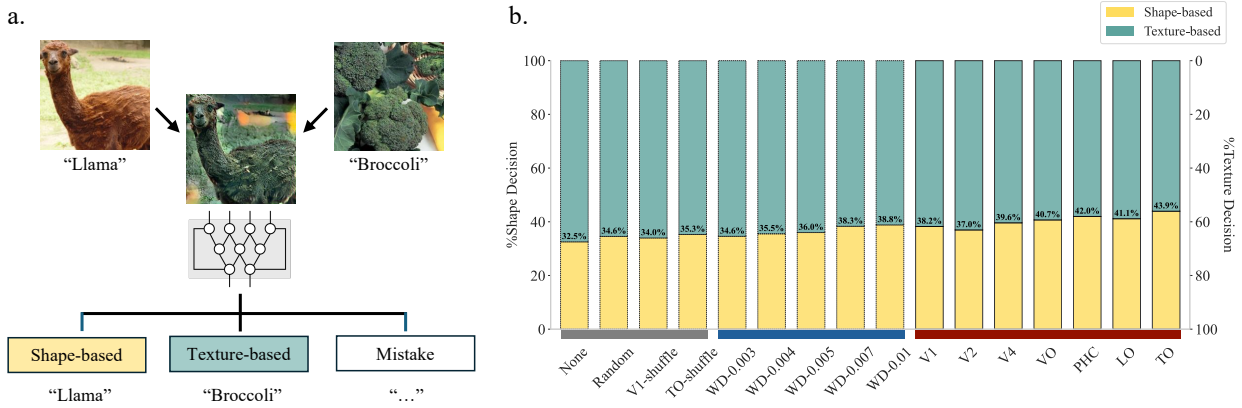


Fig 4. Neurally-guided models make higher percentages of shape-based decisions. a.

Schematic illustration of the method used to evaluate the percentage of shape- versus texture-based decisions. The texture of, for example, a broccoli image⁶ is transferred⁴¹ onto a llama image⁶ resulting in the composite image displayed in the center. This composite image was then processed by a DNN and received a label. A “llama” label indicates a shape-based decision, while a “broccoli” label signifies a texture-based decision. Any other label is classified as an incorrect response. **b.** Percentage of shape-based versus texture-based decisions made by each model, calculated after excluding incorrect responses. The five WD models are labeled according to their weight decay parameter values, such as WD-0.003, WD-0.004, etc., applied during training. The numbers shown on each bar correspond to the percentage of shape-based decisions.

Neural-guidance alters representation space

We have suggested that neural guidance takes effect via steering DNNs’ representational spaces to better align with those achieved by humans. To directly examine the representational spaces of both neurally-guided models and those trained conventionally, we first used Representational Similarity Analysis (RSA)⁴² to provide a preliminary evaluation of the similarities in representational spaces among all models. We constructed representational spaces for all 16 models, comprising seven neurally-guided, four baseline, and five WD models (detailed methods are provided in the “Analysis” section in Methods). A secondary space similarity index, Spearman’s ρ correlation was then computed for all possible model pairs to produce the final Representation Similarity Matrix (RSM) shown in Fig 5a. In addition, we also applied

Multidimensional Scaling (MDS) to project representational space distances onto a two-dimensional plane for a clearer visualization of the similarity relationship among all models (Fig. 5b).

The RSM and MDS plots reveal notable patterns. All baseline models (with the exception of the random model) and WD models exhibit a high degree of correlation amongst themselves, indicating high representational similarity among the conventional models. Importantly, however, the neurally-guided models were less similar to, or farther away from both the baseline and WD models, underscoring a fundamental shift in their representational spaces away from conventionally trained DNNs.

The high similarity observed among the representational spaces of the conventionally trained DNNs (baseline and WD-models as depicted in the RSM), may explain the known susceptibility of DNNs to transfer attacks, that is, attacks where adversarial examples crafted for one model can compromise another. Such transferability has been consistently observed across various architectures⁴³, tasks⁴⁴, and training datasets⁴⁵. The success of transfer attacks suggests that vulnerabilities in the output space of one model often coincide with those in other models, evidencing a fundamental homogeneity among standard DNNs.

Importantly, however, if neural guidance indeed alters the representational space relative to those produced by conventional DNNs, then they may be less susceptible to such transfer attacks. This is indeed supported by the observation that neurally-guided models were less susceptible to adversarial examples generated using the None baseline model, than were the other baseline models (Supp. Fig. S3a). Interestingly, models guided by later ventral stream regions are increasingly resilient to the transfer attack. One might be tempted to consider hierarchical improvement as simply a reflection of increasing smoothness of the output surface, a characteristic also shared with WD-models with increasing smoothness regularizations (Supp. Fig. S3b); after all, increased smoothness generally leads to fewer vulnerabilities to be exploited. However, at comparable levels of smoothness scores, quantified using the magnitude of the gradient norm as previously described, neurally-guided models not only consistently outperform WD-models in resisting transfer attacks, but that resistance is more stable across various

smoothness levels (Fig. 5c). Thus, the neurally-guided models’ improved robustness to transfer attack cannot be solely attributed to smoothness per se, but instead must reflect a fundamentally different representational landscape than conventional methods, while being optimized for robustness. Thus, the core of the neurally-guided models’ robustness, guided by the inherently robust human visual system, likely stems from their unique representational spaces transformed with principles distinct from those of conventional DNN structures.

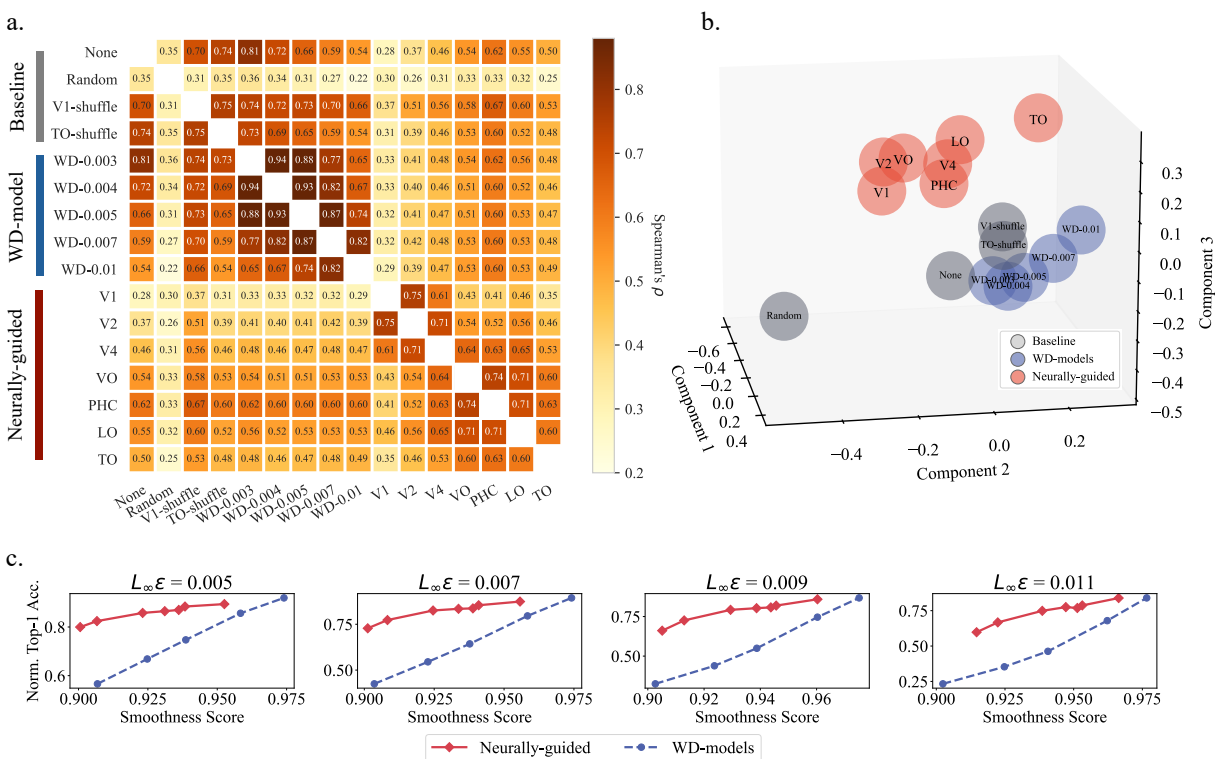


Fig 5. Neurally-guided DNNs’ representational spaces and output surfaces are different from standard models. **a.** Heatmap from Representation Similarity Analysis (RSA) depicting the similarity in representation spaces across all models. Each cell represents the similarity between two models, quantified by Spearman’s ρ , where a higher value signifies a greater correlation. Diagonal elements, always denoting self-correlation with a value of 1, have been masked. **b.** Multidimensional Scaling (MDS) visualization based on the Representational Similarity Matrix (RSM) presented in **a**. Each circle represents one of the 16 models evaluated, where proximity indicates similarity in the representational space of each model. **c.** Relationship between transfer attack top-1 classification accuracy (normalized to each model’s accuracy on

clean images) and smoothness scores, for both neurally-guided models and WD-models, depicted across four different l_∞ -based neighborhood radii. Points representing WD-models correspond to models trained with specific weight decay values, whereas points for neurally-guided models correspond to those guided by distinct ROIs.

Discussion

Our results reveal a hierarchical enhancement in DNN robustness when their representational learning is guided by progressively later regions along the human ventral visual stream. Such hierarchical improvement persists across various types of adversarial attacks, input datasets, and tasks. The resulting representational spaces are both increasingly shape-biased and smooth. Importantly, though, neural guidance differs from more conventional methods of inducing smooth decision surfaces in that neural guidance ultimately leads to less susceptibility to transfer attacks. Our results not only support the crucial role of the ventral visual stream in gradually achieving resilience via, for example, producing increasingly disentangled manifolds⁹ but also suggest that neural-guidance produces a qualitatively different and superior approach to robustness than conventional methods.

Despite its early stage in the visual processing hierarchy, even models guided by V1 showed notable improvements in robustness. Given that fMRI lacks the temporal resolution to precisely track the dynamics of representational transformation, it remains an open question as to whether these initial improvements are inherent to the features initially extracted by V1²⁶ or a result of subsequent, higher-level feedback enhancing early representations⁴⁶. Interestingly, V2 did not confer further benefits beyond those observed with V1, and in some analyses such as the texture-shape bias and smoothness evaluation, V2 resulted in worse performance. Such results may be related to V2's role in texture segmentation⁴⁷. However, further investigation into V2's specific contributions to the resilience of the visual system is needed.

The TO region is a motion-sensitive area that is sometimes referred to as the human MT+ complex⁴⁸. We included TO along with LO to collectively capture the more anterior and more posterior sections of the functionally defined LOC²⁹. Although TO is less often investigated in the context of visual recognition, it has been implicated in the processing of three-dimensional

shape⁴⁹⁻⁵¹. We also extended our analysis to VO (Ventral-Occipital) and the PHC (Posterior Parahippocampal Cortex). Although these regions demonstrated enhanced performance compared to LO, neither matched the efficacy observed in TO (Fig. 2b). It is unclear whether this difference is attributed TO's role in shape processing or whether TO's superior performance is a result of the higher quality fMRI signal, as demonstrated by both higher noise ceiling (Supp. Fig. S4), indicating a greater proportion of signal variance attributable to the stimulation rather than measurement noise, and the more accurate prediction capability of the TO neural predictor (Fig. 1c).

As discussed, our findings are consistent with theories that all identity-preserving changes to objects form continuous representation manifolds^{9,52}. These manifolds are highly entangled in their native pixel space but gradually become more distinguishable through the ventral stream's successive stages. Such separation of manifolds, therefore, leads naturally to invariance⁹. With adequately separated manifolds, local smoothness is less critical, meaning that minor changes to a correctly classified image should not alter the output decision. Similar assumptions have been made for DNNs until the advent of adversarial attacks⁸, revealing that DNNs' generalization capabilities cannot be guaranteed even within close proximity to accurately recognized images. Interestingly, the search for adversarial examples of human visual system^{53,54} has met with some success. Thus, although we do not contend that the human visual system is entirely impervious to such attacks, our findings affirm that the human visual system likely houses a superior representation space with smoother decision surfaces and better-separated object manifolds than DNNs, thus leading to the observed robustness improvement in our neurally-guided models.

Our neurally-guided models also offer the potential to uncover principles governing human vision that can then inform the development of DNNs. We observe, for instance, that their output surfaces are smoother, potentially as a result of achieving a more human-like representational space with optimized smoothness as opposed to arbitrary smoothing seen in conventional methods. This optimized smoothness not only facilitates adversarial robustness but also achieves more separable object manifolds, resulting in greater invariance to identity-preserving transformations⁹. Furthermore, the observed shape bias may be another emergent property stemming from the increasingly smooth and disentangled representational space. However, more

exploration as to how such representational space is achieved is needed. What the data presented here make clear is that the principles that enable the construction of resilient representational space are embedded in the ventral visual stream of the human cortex and understanding how the neurally-guided and conventional representational spaces differ should provide critical insights for developing the next generation of DNNs.

Methods

Neural Data

Neural data were obtained from the publicly available Natural Scene Data (NSD)²⁴. High-resolution, whole-brain functional Magnetic Resonance Imaging (fMRI) scans were collected from human participants as they viewed a selection of natural images from the MSCOCO image database⁵⁵. We used the fully preprocessed neural data and the %signal change estimates from NSD’s processing pipeline for better reproducibility. All analysis and results presented in the text are based on data from Subject-1 included in the NSD dataset, although a similar hierarchy has been observed across three other human subjects (see Supp. Fig S5 for details). Subsequent analyses, such as the extraction of Regions of Interest (ROIs) and additional data cleaning, were performed using custom scripts in AFNI (version: AFNI_23.0.0) and Python (version: 3.9.16). We used data from Subject-1 with the highest noise ceiling²⁴ ensuring the use of high-quality neural data to optimize the training process for neural predictors.

Regions-of-Interest (ROIs): ROIs were delineated using an anatomical atlas²⁵ that probabilistically assigns voxels to different topological regions within the human visual system. We focused on ROIs from V1, V2, (h)V4, LO, VO, PHC to TO. We further intersected each ROI mask with a provided “nsdgeneral” mask in NSD subject-1’s native space to ensure that the voxels used are more confined to the grey matter and visually responsive in the NSD experiment.

Functional Data: We used the 1.8mm-resolution 7T functional data to take advantage of its higher signal-to-noise ratio (SNR). In the NSD experiment, each trial consisted of a human participant viewing a single image in the scanner. A general linear model (GLM) that includes hemodynamic response function (HRF)-based regressors modeling the onset of each image and a variety of denoising regressors were fitted to each voxel’s time series to extract its activation level in response to the image appearing in a given trial. The activation level corresponds to the coefficient for the image regressors within the GLM, denoted as “ β ”, in the unit of %signal change. Within a given ROI, the β values from all voxels compose the neural representation vector for the corresponding image viewed. We used the β values obtained from the “b3” version²⁴ of the GLM that includes individually estimated HRF for each voxel, additional denoising techniques, and ridge regression to ensure optimal data quality.

Further preparation for neural predictor training: To reduce the noise in the signal, we further averaged the neural representation vectors across repetitions of the same image, when possible. There was an imbalance in repetition frequency due to the exclusion of two sessions of NSD data for the Algonauts challenge⁵⁶. For subject-1, 8,420 images were repeated three times, 1,069 images were repeated two times, and 352 images did not have any repetition, and we obtained a set of 9,841 unique images. Our train/test split adhered to the same protocol as the original NSD experiment²⁴, where a subset of randomly selected images viewed by all participants was used as the test set. This resulted in a training set comprising 8,859 MSCOCO images and their corresponding neural representations, with the remaining 982 image-neural response pairs forming the test set. Furthermore, we performed a Principal Component Analysis (PCA), only using components that explained 95% or more variance, to reduce noise and dimensionality of the neural representation vectors, thereby simplifying the subsequent training process.

Importantly PCA was first applied to the training data to determine the transformation parameters, which were then applied to the test data to avoid potential data leakage.

Neural predictors

Neural predictor architecture: Neural predictors were based on the convolutional neural network, ResNet18⁵⁷. The only structure modification was the resizing of the final fully connected (FC) layer to correspond with the dimensionality of the targeted ROI. For instance, to predict the V1 ROI with 1084 dimensions, the FC layer was reconfigured to match this with 1084 output units. All components typically associated with classification tasks, such as the softmax layer, were removed to repurpose the ResNet18 as a feature extractor. We trained seven neural predictors each acting as the surrogate for one of the seven ROIs investigated.

Architectural modification for CIFAR-100: When replicating the robustness improvements from neural guidance on CIFAR-100⁵⁸ images, we adapted the architecture of neural predictors too to address the challenge posed by the much lower resolution of CIFAR-100 images (32x32), which contrasts sharply with the higher resolution of MSCOCO images (227x227) from NSD. We trained additional seven neural predictors on down-sampled MSCOCO images while modifying the initial convolutional layer (Conv1) of the neural predictors by reducing both the kernel size (reduced from 7 to 3) and stride (reduced from 2 to 1) to better accommodate the smaller image size.

Neural predictor training: Training of neural predictors was conducted using a Mean-Squared Error (MSE) loss:

$$\min_{\phi} \sum_{i=1}^n \frac{1}{n} \|g_{\phi}(x_i) - y_i\|_2^2$$

where g_{ϕ} represents the neural predictor with parameters ϕ , x_i denotes the input image and y_i denotes its corresponding neural response vector, and n denotes the image set size used in the training. Throughout the training, we monitored the Euclidean distance and Pearson’s r correlation between the ground-truth neural representations and the predicted outputs. Upon completing the training, we fixed the weights of all neural predictors, repurposing them as feature extractors for subsequent neural-guided training. Additionally, to validate the efficacy of our neural predictors, we conducted control experiments where the network was trained on shuffled neural data. Specifically, for each input image, we assigned a randomly selected, non-corresponding neural response as the ground truth. However, the integrity of the input-output correspondence was maintained during testing. Therefore, if the correlations observed under these shuffling conditions are significantly lower than those achieved with accurately paired training data, this would confirm that the neural predictors are learning meaningful representations relevant to the image shown. Results of such training quality checks for the neural predictors are presented in Fig. 1c. We note that neural predictors trained with this shuffling process as control conditions were used only for quality check purposes and discarded before our main analysis of the neural guidance effects. Both “V1-shuffle” and “TO-shuffle” models used in the main analysis involved the use of validly trained neural predictors but with

shuffled input images to give incorrect neural-guidance (see *Neural-guided Training* section below).

Image datasets used for neural guidance

ImageNet-50: The primary dataset used in our study to assess the neural-guidance method was a subset of ImageNet that consists of 50 categories closely mirroring those found in the original MSCOCO images viewed by the human subjects. We note that the neural predictors were trained on a limited number of MSCOCO images and asked to perform a demanding representation extraction task that transfers to the ImageNet dataset. We facilitated this transfer by opting for a subset of ImageNet that bears the closest resemblance to the class labels of MSCOCO images used in the training of neural predictors. The complex and object-dense nature of MSCOCO images precludes a direct one-to-one correspondence between each image and ImageNet categories. Therefore, the selection of relevant ImageNet categories was determined by the classification outputs of a pre-trained deep neural network, specifically Resnet-101 with the latest pre-trained weights from PyTorch (version 2.0.0) on MSCOCO images used in NSD. From this process, the top 50 most frequently occurring categories in the classification results were used as our primary dataset.

CIFAR-100: To show the generality of neural guidance, we employed an additional image set, CIFAR-100⁵⁸, which is distinct in characteristics from ImageNet yet similarly purposed for classification tasks. Given the low resolution of CIFAR-100 images (32x32), we made necessary architectural adjustments to the neural predictors (detailed in the *Neural Predictors* section) and the neural-guided model (discussed in the *Neurally-guided Training* section) to accommodate these images.

MSCOCO-NSD: To evaluate the effect of neural guidance on a different task, namely image captioning, a different dataset from those used in classification tasks (ImageNet and CIFAR-100) was required. We adopted a subset of MSCOCO⁵⁵ images viewed by Subject-1 in the NSD. These images are diverse enough for the purpose of evaluation and have the advantage of having been used in the training of the neural predictor. The train/test split was the same as the division used in the training of the neural predictors.

Neurally-guided Training

Neurally-guided model architecture: Our primary model is an adaptation of ResNet-18, augmented with an additional fully-connected (FC) layer situated after the last convolutional block and the immediate average pooling layer, functioning in tandem with the original FC classification layer. This additional FC layer, or “neural head”, is configured to match the size of the targeted ROI and dedicated to learning the neural representation of each input image, while the original “task head” concentrates on the actual classification task. We note that the neural-guidance is from the fully trained neural predictors acting as surrogates to each of the seven ROIs. Fig 1a shows a visual illustration of this bifurcated structure. Seven models were trained on the ImageNet-50 dataset, each designed to learn neural representations from one of the

surrogate neural predictors. Another set of seven models with modification done to the initial convolution layer in the same fashion as discussed in the *Neural predictors* section were trained on the CIFAR-100 dataset to account the reduced resolution of these images.

Neurally-guided classification training: During training, the neural-guided models were tasked with learning both the neural representation and the classification task concurrently. The architecture of the neural-guided models composes three parts (Fig. 1a): the shared backbone f^s , the task head f^t , and the neural head f^n . The combined training objective is:

$$\min_{\theta_1, \theta_2, \theta_3} \sum_{i=1}^N \frac{1}{N} \ell(f_{\theta_2}^t(z_i) - y_i) + \alpha \cdot \frac{1}{N} \|f_{\theta_3}^n(z_i) - g_{\phi}(x_i)\|_2^2$$

where $z_i = f_{\theta_1}^s(x_i)$ denotes the output of the shared backbone, and $\theta_1, \theta_2, \theta_3$ are the parameters of f^s, f^t, f^n , respectively. ℓ represents the task loss function e.g. cross-entropy loss for classification task. The hyperparameter α was tuned to achieve an optimal balance between the performance of the neural representation learning and the classification task.

Baseline models: We trained four additional baseline models, each designed to test alternative hypothesis of the neural guidance effect. The “None” model, serving as the absolute baseline condition, has only the task head and was merely fine-tuned on the training datasets. The “Random” model has a dual-headed structure, but the neural head was guided by the output of an untrained neural predictor with randomly initialized weights and can be used to test if the mere addition of an uninformative neural head could lead to improvement. The “V1-shuffle” and “TO-shuffle” models were both informed by the outputs of correctly trained V1 and TO neural predictors, respectively. However, during the neural-guided training, we shuffled the input images to the neural predictors so that the resulting predicted neural representation used as guidance was mismatched with the original input image fed into the main model. This shuffling intended to determine whether any observed improvement in robustness could be attributed to neural-characteristic noise rather than to genuine informational content.

Image captioning

To ask if the features extracted by neural-guided models can lead to improvement for tasks beyond classification, we employed an image captioning task using the MSCOCO-NSD dataset relying on features extracted by trained neural-guided models. Following the common encoder-decoder framework³⁵, our encoder consisted of the neural-guided models trained on ImageNet-50 classification task, after removing the neural head, the task head, and the average pooling layer immediately following the fourth convolution block. The extracted features with the spatial structure retained were fed into the decoder which consisted of a Long-Short-Term-Memory (LSTM) layer for generating image captions, supplemented by an attention module to improve performance. Decoder initialization employed pre-trained weights³⁵ and was finetuned on the MSCOCO-NSD dataset with features extracted by neurally-guided models. The loss function for image captioning finetuning was defined as

$$L = - \sum_t \log P(y_t | a, y_{1:t-1})$$

where y_t denotes the word to be generated at time t , $y_{1:t-1}$ denotes the sequence of words generated up to time $t - 1$, and a represents the set of annotation vectors extracted from the image by the DNN encoder. The probability of the word at time t then is:

$$P(y_t|a, y_{1:t-1}) \propto \exp(L_0(E_{y_{t-1}} + L_h h_t + L_z \hat{z}_t)),$$

Where L_0, L_h, L_z are learned parameters, $E_{y_{t-1}}$ is the embedding of the previously generated word, h_t is the hidden state of the Recurrent Neural Network (RNN) in the decoder at time t , and \hat{z}_t is the context vector at time t , calculated as a weighted sum of the annotation vector a . The weights for the weighted sum are determined by the attention mechanism, based on the current hidden state h_t and a . The performance of the captioning task was then assessed using the conventional BLEU scores⁵⁹.

Adversarial Attacks:

When evaluating the adversarial robustness of models, the neural head was removed from all neural-guided models, focusing the attack only on the task head. Specifically, for each specific image X_i , we search for a perturbation τ that could be added to X_i without exceeding a maximum perturbation magnitude threshold, ϵ , as measured by a specified l_p norm:

$$\max_{\|\tau\|_p \leq \epsilon} \ell_p(f_\theta(x_i + \tau), y_i)$$

We included a range of ϵ to show the robustness difference across different attack strengths (Fig. 2b). The primary attack method employed was the l_∞ -based Projected Gradient Descent (PGD) attack³¹. Since we focus on the robustness improvement of models, instead of the absolute accuracy level, we normalized each model’s task accuracy with respect to their performance on clean image sets using: $1 - \left| \frac{acc_{adv} - acc_{clean}}{acc_{clean}} \right|$. To ensure that the observed robustness

improvements attributed to neural guidance were not merely a coincidental result of l_∞ -based PGD attack, we subjected the models to a range of common adversarial attacks, including: 1. l_∞ -based AutoAttack³³, which aggregates several attack methods including FAB, Square Attack, APGD-CE, and APGD-DLR; 2. l_∞ -based Fast Gradient Sign Method (FGSM)⁶⁰; 3. l_2 -based Fast Gradient Method (FGM) attack^{60,61}; and 4. l_2 -based DeepFool attack³⁴.

Analysis:

Smoothness evaluation: We visualized the model’s loss landscape with respect to an input image using the following procedure. For a given input data x , ground truth y , and the loss function ℓ_θ , we first compute the two leading eigenvectors v_1, v_2 of the Hessian matrix $H = \frac{\partial^2 \ell_\theta(x, y)}{\partial x^2}$, then construct the perturbed image as

$$\hat{x} = x + \delta_1 v_1 + \delta_2 v_2,$$

and plot the relation between δ_1, δ_2 , and $\ell_\theta(\hat{x}, y)$. The leading eigenvectors are computed using power iterations⁶². We further quantified the models’ smoothness loss³⁷ as the “worst” smoothness in a given data point x ’s l_∞ -based neighborhood:

$$\mathcal{L}_{smooth}(\ell, \theta, x, y) = \max_{\|\hat{x} - x\|_\infty \leq \epsilon} \|\nabla_{\hat{x}} \ell_\theta(\hat{x}, y)\|_2$$

In practice, we leveraged projection gradient descent (PGD) optimization to search for an adversarial image \hat{x} , then calculate the gradient norm³⁷ of the loss with respect to \hat{x} . Note that for

this quantification, higher values suggest larger gradients, steeper slopes, and therefore less smooth surfaces. For clarity, we applied the following transformation: $e^{-\mathcal{L}_{smooth}}$ so that higher smoothness scores correspond to a smoother output surface.

Standard training with smoothness regularization: To demonstrate that neural-guided models achieve a smoother loss landscape that differs from conventional smoothness regularization techniques, we trained additional ResNet-18 models (“WD-models”) on the ImageNet-50 dataset. These models were specifically adjusted for smoothness by varying the weight decay parameter³⁹, a common method for imposing regularization. For a better comparison, we selected five distinct weight decay values, targeting smoothness levels within a range comparable to those observed in neural-guided models, as shown in Figure 5b and Supp Fig. S2. The evaluation of smoothness scores for these WD-models was conducted using the same methodology applied to the neural-guided models.

Texture-shape bias: To assess the texture-shape bias of our neural-guided models, we employed a similar methodology as in previous work⁴⁰, performing style transfer⁴¹ across different categories within the ImageNet-50 dataset, and evaluated the classification outputs. This process involved randomly selecting pairs of images from different categories, and then merging the pair to create an image with texture of one category and the shape of another. The resultant style-transferred images were then subjected to classification by the neural-guided models. The models’ responses can be divided into three possible outcomes: a shape-based decision (aligning with human behavior⁴⁰), a texture-based decision (a pattern commonly observed in DNNs), or an incorrect decision. This analysis enabled us to quantify the models’ inclination for shape versus texture decisions, as shown in Fig. 4.

Representational space similarity: We applied Representation Similarity Analysis (RSA)⁴² to assess the similarity of the representational spaces of all WD-models, neurally-guided models, and baseline models. We used the MSCOCO images presented to participants in the NSD experiment to construct the representational spaces. For all ResNet18-based DNN models, we extracted 1D feature vectors from the average-pooling layer corresponding to these MSCOCO images to construct each model’s representation spaces. We then calculated the Euclidean distance between all possible pairs of image features to form a Representational Dissimilarity Matrix (RDM) for each model. Subsequently, we computed pair-wise Spearman’s ρ correlations to generate a final matrix representing the similarity of representation spaces (Fig. 5a), i.e., the Representational Similarity Matrix (RSM). Higher correlations, indicated by darker colors, correspond to greater similarity between the representation spaces of two entities (models). For a more intuitive visualization of the similarity relationship among all models, we further applied Multidimensional Scaling (MDS). The RSM was first converted to a distance matrix using $1 - \text{RSM}$, and then reduced to two principal dimensions using the scikit-learn library⁶³ (version 1.0.2). The resulting two-dimensional representation preserves the pairwise dissimilarities between models such that those with more similar representational spaces appear closer together in the plot (Fig. 5b).

Transfer attack: To further assess the similarity of the loss landscape with respect to input images between neural-guided models and conventionally trained models, we employed transfer attacks⁶⁰ as an alternative evaluative measure. Specifically, adversarial examples were generated

by attacking the standard “None” model, which had undergone only fine-tuning on the ImageNet-50 dataset, using the l_∞ -based PGD attack. These adversarial examples were then applied to both the set of five WD-models and the seven neural-guided models to evaluate their classification accuracy on these perturbed inputs. Poor accuracy then indicates compromised performance and thus a greater similarity in the loss landscape, or more precisely, the positioning of adversarial examples, between the source “None” model and the target model.

Acknowledgements: This work used NCSA Delta GPU through allocation SOC230011 from the Advanced Cyberinfrastructure Coordination Ecosystem: Services & Support (ACCESS) program, which is supported by National Science Foundation grants #2138259, #2138286, #2138307, #2137603, and #2138296.

Author Contributions: Z. S., L. M, B. L., and D. M. B. conceived and designed the analysis. Z. S. and L. M. performed the analysis. Z. S. and L. M. wrote the paper. B. L. and D. M. B. supervised the project. All authors made edits, reviewed the results, and approved the final version of the manuscript.

Competing Interests: The authors declare no conflicts of interest.

Code availability: Source codes are available at: github.com/shaox192/NeuralGuidance.

Data availability: All recordings of human neural data were obtained from the publicly available dataset: Natural Scene Dataset²⁴.

References

1. Biederman, I. & Cooper, E. E. Evidence for Complete Translational and Reflectional Invariance in Visual Object Priming. *Perception* **20**, 585–593 (1991).
2. Biederman, I. & Gerhardstein, P. C. Recognizing depth-rotated objects: Evidence and conditions for three-dimensional viewpoint invariance. *J. Exp. Psychol. Hum. Percept. Perform.* **19**, 1162–1182 (1993).
3. Biederman, I. & Cooper, E. E. Size invariance in visual object priming. *J. Exp. Psychol. Hum. Percept. Perform.* **18**, 121–133 (1992).
4. Geirhos, R. *et al.* Generalisation in humans and deep neural networks. in *Advances in Neural Information Processing Systems* vol. 31 (Curran Associates, Inc., 2018).
5. Bowers, J. S., Vankov, I. I. & Ludwig, C. J. H. The visual system supports online translation invariance for object identification. *Psychon. Bull. Rev.* **23**, 432–438 (2016).
6. Russakovsky, O. *et al.* ImageNet Large Scale Visual Recognition Challenge. *Int. J. Comput. Vis.* **115**, 211–252 (2015).
7. Bowers, J. S. *et al.* Deep problems with neural network models of human vision. *Behav. Brain Sci.* 1–74 (2022) doi:10.1017/S0140525X22002813.
8. Szegedy, C. *et al.* Intriguing properties of neural networks. Preprint at <http://arxiv.org/abs/1312.6199> (2014).
9. DiCarlo, J. J. & Cox, D. D. Untangling invariant object recognition. *Trends Cogn. Sci.* **11**, 333–341 (2007).
10. Fukushima, K. & Miyake, S. Neocognitron: A new algorithm for pattern recognition tolerant of deformations and shifts in position. *Pattern Recognit.* **15**, 455–469 (1982).

11. Biscione, V. & Bowers, J. S. Convolutional neural networks are not invariant to translation, but they can learn to be. *J. Mach. Learn. Res.* **22**, 1–28 (2021).
12. Hendrycks, D. & Dietterich, T. Benchmarking neural network robustness to common corruptions and perturbations. Preprint at <http://arxiv.org/abs/1903.12261> (2019).
13. Dong, Y. *et al.* ViewFool: Evaluating the robustness of visual recognition to adversarial viewpoints. *Adv. Neural Inf. Process. Syst.* **35**, 36789--36803 (2022).
14. Papernot, N., McDaniel, P., Sinha, A. & Wellman, M. P. SoK: Security and Privacy in Machine Learning. in *2018 IEEE European Symposium on Security and Privacy (EuroS&P)* 399–414 (2018). doi:10.1109/EuroSP.2018.00035.
15. Rust, N. C. & DiCarlo, J. J. Selectivity and Tolerance (“Invariance”) Both Increase as Visual Information Propagates from Cortical Area V4 to IT. *J. Neurosci.* **30**, 12978–12995 (2010).
16. Jordan, M. C., Greene, M. R., Beck, D. M. & Fei-Fei, L. Basic level category structure emerges gradually across human ventral visual cortex. *J. Cogn. Neurosci.* **27**, 1427–1446 (2015).
17. Serre, T., Oliva, A. & Poggio, T. A feedforward architecture accounts for rapid categorization. *Proc. Natl. Acad. Sci.* **104**, 6424–6429 (2007).
18. Bao, P., She, L., McGill, M. & Tsao, D. Y. A map of object space in primate inferotemporal cortex. *Nature* **583**, 103–108 (2020).
19. Quiroga, R. Q., Reddy, L., Kreiman, G., Koch, C. & Fried, I. Invariant visual representation by single neurons in the human brain. *Nature* **435**, 1102–1107 (2005).
20. Zoccolan, D., Kouh, M., Poggio, T. & DiCarlo, J. J. Trade-Off between Object Selectivity and Tolerance in Monkey Inferotemporal Cortex. *J. Neurosci.* **27**, 12292–12307 (2007).

21. Li, Z. *et al.* Learning from brains how to regularize machines. in *Advances in Neural Information Processing Systems* vol. 32 (Curran Associates, Inc., 2019).
22. St-Yves, G., Allen, E. J., Wu, Y., Kay, K. & Naselaris, T. Brain-optimized deep neural network models of human visual areas learn non-hierarchical representations. *Nat. Commun.* **14**, 3329 (2023).
23. Dapello, J. *et al.* Aligning model and macaque inferior temporal cortex representations improves model-to-human behavioral alignment and adversarial robustness. *Int. Conf. Learn. Represent.* (2022) doi:10.1101/2022.07.01.498495.
24. Allen, E. J. *et al.* A massive 7T fMRI dataset to bridge cognitive neuroscience and artificial intelligence. *Nat. Neurosci.* **25**, 116–126 (2022).
25. Wang, L., Mruczek, R. E. B., Arcaro, M. J. & Kastner, S. Probabilistic Maps of Visual Topography in Human Cortex. *Cereb. Cortex* **25**, 3911–3931 (2015).
26. Marr, D. *Vision: A Computational Investigation into the Human Representation and Processing of Visual Information.* (MIT Press, 2010).
27. Brewer, A. A., Liu, J., Wade, A. R. & Wandell, B. A. Visual field maps and stimulus selectivity in human ventral occipital cortex. *Nat. Neurosci.* **8**, 1102–1109 (2005).
28. Arcaro, M. J., McMains, S. A., Singer, B. D. & Kastner, S. Retinotopic organization of human ventral visual cortex. *J. Neurosci.* **29**, 10638–10652 (2009).
29. Larsson, J. & Heeger, D. J. Two Retinotopic Visual Areas in Human Lateral Occipital Cortex. *J. Neurosci.* **26**, 13128–13142 (2006).
30. Grill-Spector, K. *et al.* Differential processing of objects under various viewing conditions in the human lateral occipital complex. *Neuron* **24**, 187–203 (1999).

31. Madry, A., Makelov, A., Schmidt, L., Tsipras, D. & Vladu, A. Towards deep learning models resistant to adversarial attacks. Preprint at <http://arxiv.org/abs/1706.06083> (2019).
32. Goodfellow, I. J., Shlens, J. & Szegedy, C. Explaining and harnessing adversarial examples. Preprint at <http://arxiv.org/abs/1412.6572> (2015).
33. Croce, F. & Hein, M. Reliable evaluation of adversarial robustness with an ensemble of diverse parameter-free attacks. Preprint at <https://doi.org/10.48550/arXiv.2003.01690> (2020).
34. Moosavi-Dezfooli, S.-M., Fawzi, A. & Frossard, P. DeepFool: a simple and accurate method to fool deep neural networks. Preprint at <http://arxiv.org/abs/1511.04599> (2016).
35. Xu, K. *et al.* Show, Attend and Tell: Neural Image Caption Generation with Visual Attention. in *Proceedings of the 32nd International Conference on Machine Learning 2048–2057* (PMLR, 2015).
36. Cohen, J. M., Rosenfeld, E. & Kolter, J. Z. Certified adversarial robustness via randomized smoothing. *Int. Conf. Mach. Learn. ICML* 1310--1320 (2019).
37. Yang, Z. *et al.* TRS: Transferability Reduced Ensemble via Promoting Gradient Diversity and Model Smoothness. in *Advances in Neural Information Processing Systems* vol. 34 17642–17655 (Curran Associates, Inc., 2021).
38. Rosca, M., Weber, T., Gretton, A. & Mohamed, S. A case for new neural network smoothness constraints. in 21–32 (PMLR, 2020).
39. Loshchilov, I. & Hutter, F. Decoupled weight decay regularization. Preprint at <https://doi.org/10.48550/arXiv.1711.05101> (2019).
40. Geirhos, R. *et al.* ImageNet-trained CNNs are biased towards texture; increasing shape bias improves accuracy and robustness. Preprint at <https://doi.org/10.48550/arXiv.1811.12231> (2022).

41. Gatys, L. A., Ecker, A. S. & Bethge, M. Image style transfer using convolutional neural networks. in *2016 IEEE Conference on Computer Vision and Pattern Recognition (CVPR)* 2414–2423 (IEEE, Las Vegas, NV, USA, 2016). doi:10.1109/CVPR.2016.265.
42. Kriegeskorte, N. Representational similarity analysis – connecting the branches of systems neuroscience. *Front. Syst. Neurosci.* (2008) doi:10.3389/neuro.06.004.2008.
43. Papernot, N., McDaniel, P. & Goodfellow, I. Transferability in machine learning: From phenomena to black-box attacks using adversarial samples. Preprint at <http://arxiv.org/abs/1605.07277> (2016).
44. Lu, Y. *et al.* Enhancing cross-task black-box transferability of adversarial examples with dispersion reduction. in *2020 IEEE/CVF Conference on Computer Vision and Pattern Recognition (CVPR)* 937–946 (IEEE, Seattle, WA, USA, 2020). doi:10.1109/CVPR42600.2020.00102.
45. Richards, L. E. *et al.* Adversarial Transfer Attacks With Unknown Data and Class Overlap. in *Proceedings of the 14th ACM Workshop on Artificial Intelligence and Security* 13–24 (ACM, Virtual Event Republic of Korea, 2021). doi:10.1145/3474369.3486862.
46. Lee, T. S., Mumford, D., Romero, R. & Lamme, V. A. The role of the primary visual cortex in higher level vision. *Vision Res.* **38**, 2429–2454 (1998).
47. Anzai, A., Peng, X. & Van Essen, D. C. Neurons in monkey visual area V2 encode combinations of orientations. *Nat. Neurosci.* **10**, 1313–1321 (2007).
48. Amano, K., Wandell, B. A. & Dumoulin, S. O. Visual field maps, population receptive field sizes, and visual field coverage in the human MT+ complex. *J. Neurophysiol.* **102**, 2704–2718 (2009).

49. Freud, E., Culham, J. C., Plaut, D. C. & Behrmann, M. The large-scale organization of shape processing in the ventral and dorsal pathways. *eLife* **6**, e27576.
50. Thompson, J. C. & Baccus, W. Form and motion make independent contributions to the response to biological motion in occipitotemporal cortex. *NeuroImage* **59**, 625–634 (2012).
51. Georgieva, S. S., Todd, J. T., Peeters, R. & Orban, G. A. The extraction of 3D shape from texture and shading in the human brain. *Cereb. Cortex* **18**, 2416–2438 (2008).
52. DiCarlo, J. J., Zoccolan, D. & Rust, N. C. How does the brain solve visual object recognition? *Neuron* **73**, 415–434 (2012).
53. Guo, C. *et al.* Adversarially trained neural representations are already as robust as biological neural representations. in *Proceedings of the 39th International Conference on Machine Learning* 8072–8081 (PMLR, 2022).
54. Elsayed, G. *et al.* Adversarial examples that fool both computer vision and time-limited humans. in *Advances in Neural Information Processing Systems* vol. 31 (Curran Associates, Inc., 2018).
55. Lin, T.-Y. *et al.* Microsoft COCO: Common Objects in Context. in *Computer Vision – ECCV 2014* (eds. Fleet, D., Pajdla, T., Schiele, B. & Tuytelaars, T.) 740–755 (Springer International Publishing, Cham, 2014). doi:10.1007/978-3-319-10602-1_48.
56. Gifford, A. T. *et al.* The Algonauts Project 2023 Challenge: How the Human Brain Makes Sense of Natural Scenes. Preprint at <https://doi.org/10.48550/arXiv.2301.03198> (2023).
57. He, K., Zhang, X., Ren, S. & Sun, J. Deep residual learning for image recognition. in *2016 IEEE Conference on Computer Vision and Pattern Recognition (CVPR)* 770–778 (2016). doi:10.1109/CVPR.2016.90.

58. Krizhevsky, A. Learning multiple layers of features from tiny images. (University of Toronto, 2009).
59. Papineni, K., Roukos, S., Ward, T. & Zhu, W.-J. Bleu: A method for automatic evaluation of machine translation. in *Proceedings of the 40th Annual Meeting of the Association for Computational Linguistics* (eds. Isabelle, P., Charniak, E. & Lin, D.) 311–318 (Association for Computational Linguistics, Philadelphia, Pennsylvania, USA, 2002).
doi:10.3115/1073083.1073135.
60. Goodfellow, I. J., Shlens, J. & Szegedy, C. Explaining and Harnessing Adversarial Examples. Preprint at <http://arxiv.org/abs/1412.6572> (2015).
61. Rauber, J., Brendel, W. & Bethge, M. Foolbox: A Python toolbox to benchmark the robustness of machine learning models. Preprint at <https://doi.org/10.48550/arXiv.1707.04131> (2018).
62. Yao, Z., Gholami, A., Keutzer, K. & Mahoney, M. W. PyHessian: Neural Networks Through the Lens of the Hessian. in *2020 IEEE International Conference on Big Data (Big Data)* 581–590 (2020). doi:10.1109/BigData50022.2020.9378171.
63. Pedregosa, F. *et al.* Scikit-learn: machine learning in Python. *J. Mach. Learn. Res.* **12**, 2825–2830 (2011).

Supplementary Information for

Leveraging the Human Ventral Visual Stream to Improve Neural Network Robustness

Authors: Zhenan Shao^{1,2,3,†,*}, Linjian Ma^{3,†}, Bo Li^{3,4}, Diane M. Beck^{1,2}

¹Department of Psychology, University of Illinois Urbana Champaign

²The Beckman Institute, University of Illinois Urbana Champaign

³Department of Computer Science, University of Illinois Urbana Champaign

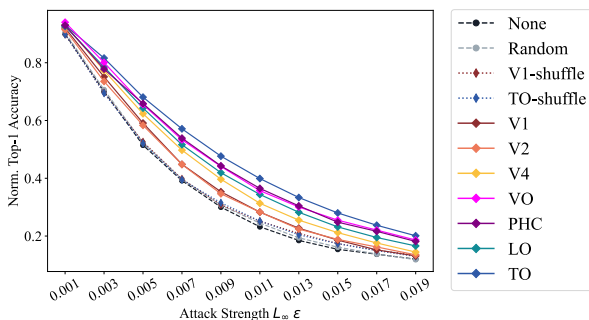
⁴Department of Computer Science, University of Chicago

*Correspondence: zhenans2@illinois.edu

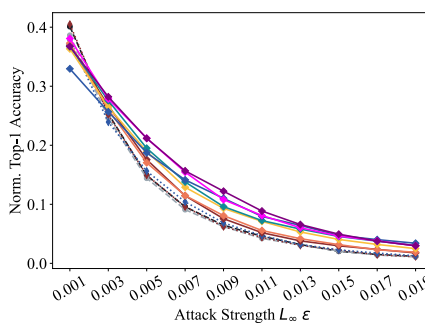
†These authors contributed equally to this work

Figure S1

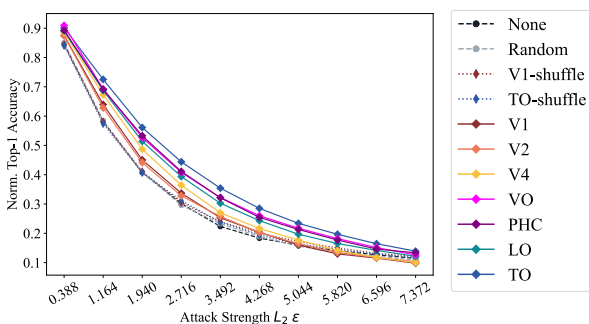
a. L_∞ FGSM attack



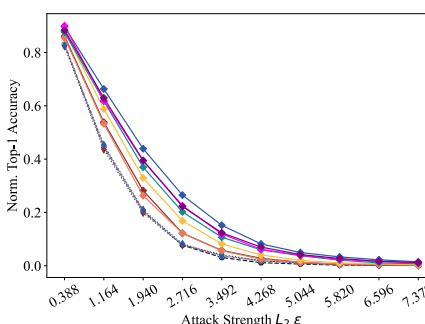
b. L_∞ Auto-attack



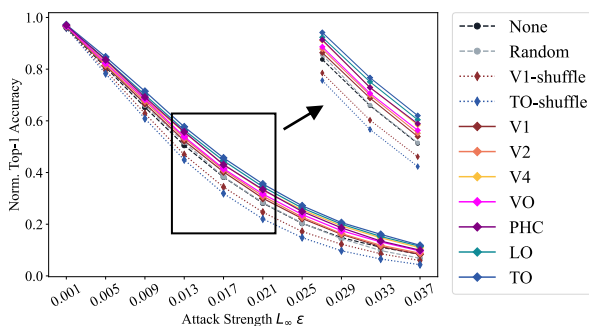
c. L_2 FGM attack



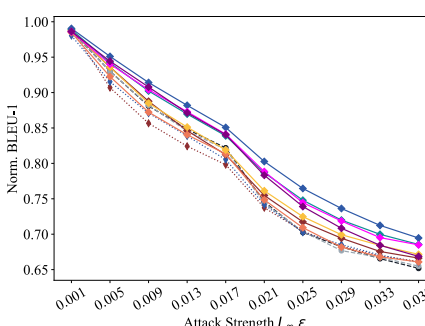
d. L_2 Deepfool attack



e. CIFAR-100 (L_∞ PGD attack)

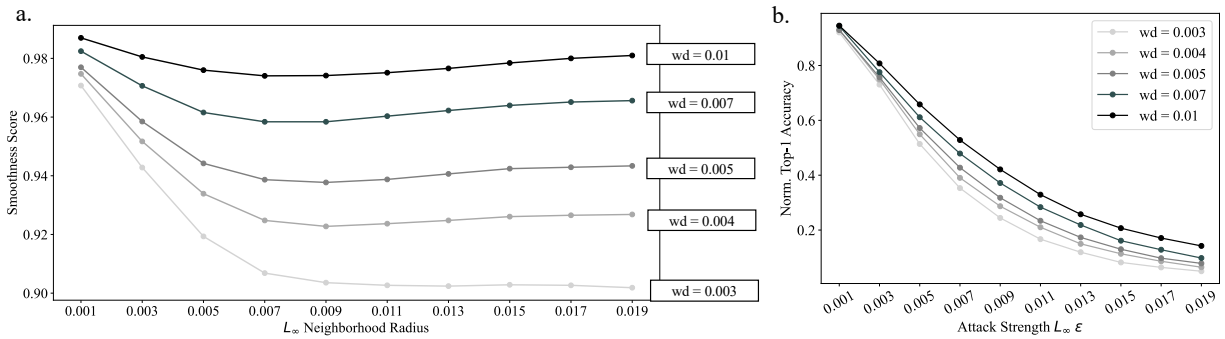


f. MSCOCO Captioning (L_∞ PGD attack)



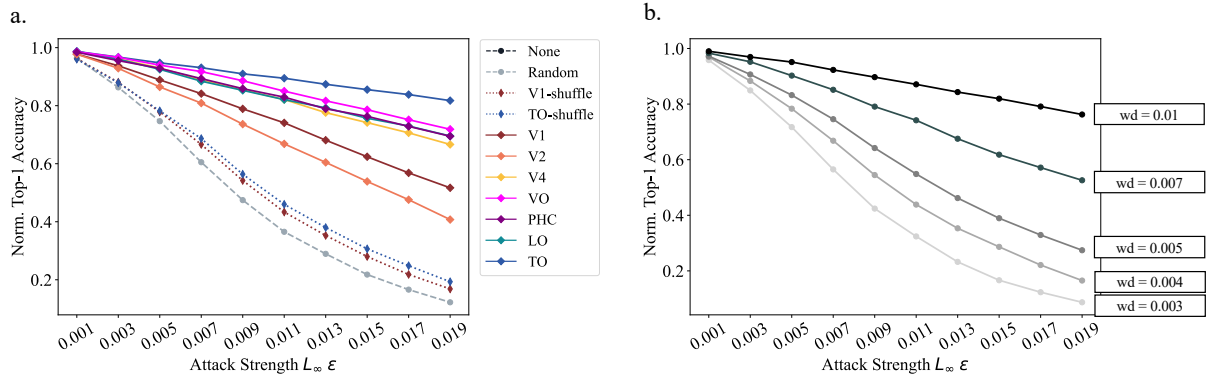
Hierarchical robustness improvement observed across different adversarial attacks, datasets, and tasks. **a. – d.** Performance of neural-guided and baseline models, all trained on the ImageNet dataset for classification L_2 tasks, but subsequently evaluated against a variety of adversarial attacks (See “Methods” in the manuscript for details). The observed hierarchy in robustness is consistent across these evaluations, despite differences in absolute accuracy scores. **e.** Performance of neural-guided and baseline models trained with classification task on the CIFAR-100¹ image set, under the L_∞ -based PGD attack². The black square and arrow indicate a blow-up window to better visualize the performance of each model on the top-right corner. **f.** Performance on image captioning task when encoders are substituted with either neural-guided or baseline models. Robustness is evaluated through the L_∞ -PGD attack. The evaluation metric used here is the BLEU-1 score to measure caption quality.

Figure S2



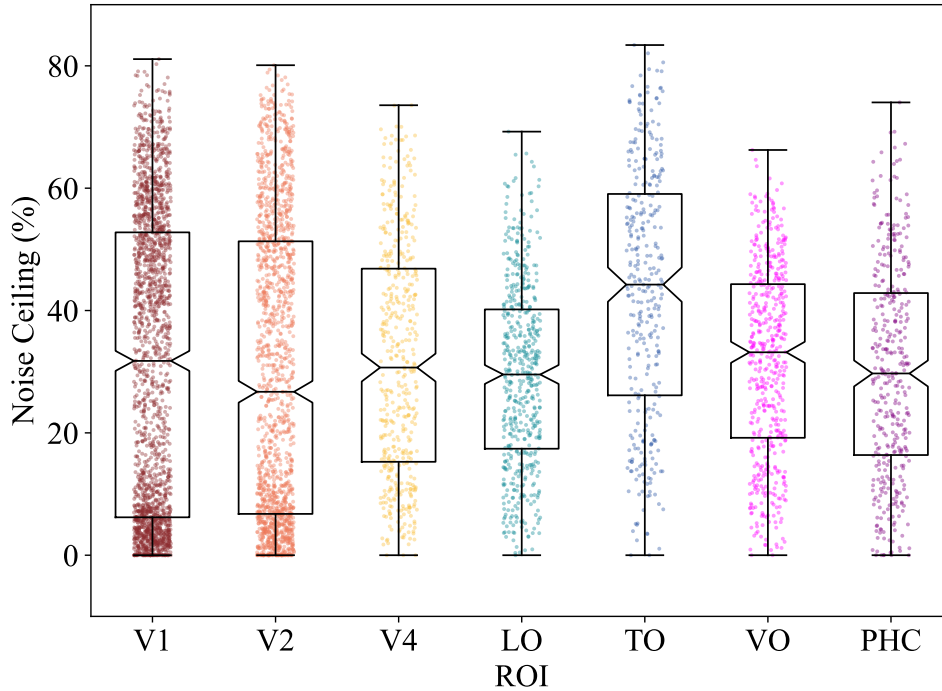
Properties of ResNet18³-based DNNs trained with varying weight decay (WD)⁴ parameters. Adjusting the weight-decay parameter is a mechanistic approach to enhancing robustness⁵, and we show both smoothness scores and adversarial robustness to confirm its effectiveness. **a.** Smoothness scores² across the five WD-models we trained. When comparing with Fig. 3b from the main text, we show that these specific WD values can yield models whose smoothness values span a comparable range to that of neural-guided models. **b.** The performance of WD-models subjected to the L_∞ -based PGD attack⁶, demonstrating a gradient of performance that corresponds with increased model smoothness due to larger penalization from higher weight decay values.

Figure S3



Transfer attack⁷ performance for neural-guided models, baseline models, and WD⁴-models, assessed using adversarial examples generated from the None-model—a standard ResNet-18 DNN trained on the ImageNet classification task. **a.** Transfer attack performance of each neural-guided model and baseline models. Higher accuracy corresponds to less transferable adversarial examples from the standard model. **b.** Transfer attack performance for all WD-models.

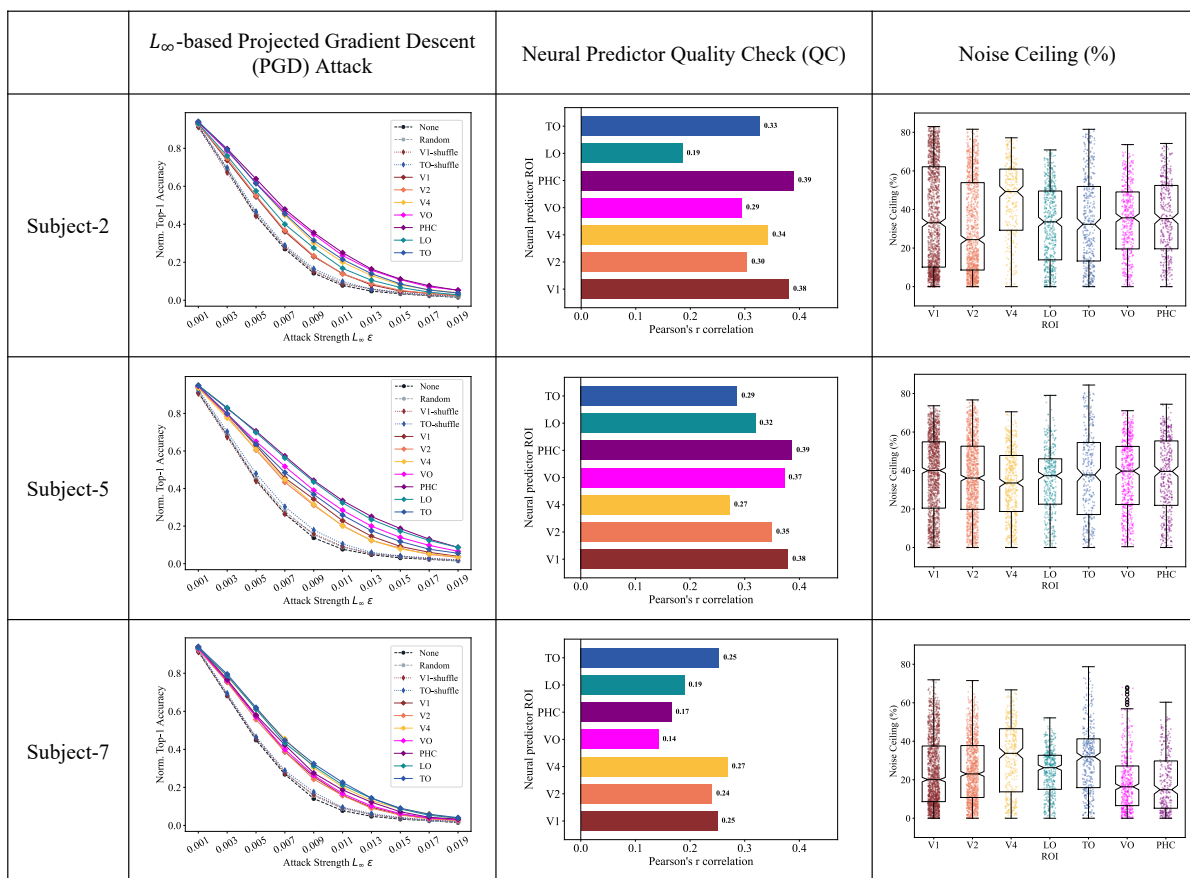
Figure S4



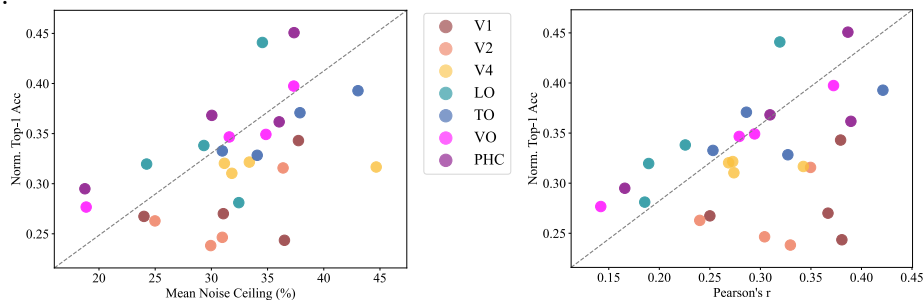
Boxplot of noise ceiling estimates for neural data from Subject-1 across seven ROIs were determined using the same procedure from the NSD experiment⁸. The center line represents the median. The edges of the box indicate the upper and lower quartiles, respectively. The whiskers extend to 1.5 times the interquartile range (IQR) from the upper and lower quartiles. Each dot represents a data point corresponding to one voxel in the corresponding ROI. Specifically, for each voxel, β values for each voxel were first standardized across all trials within each scan session to mitigate session-specific variance. Noise and signal standard deviations were derived from the three repetitions of images shown to human participants. As mentioned in the Methods section of the manuscript, the neural dataset has an imbalanced number of repetitions across images at the time of our experiment. Therefore, for the estimation of the noise ceiling estimates, we only kept the images with full three repetitions. The noise ceiling then represents the proportion of total variance in data attributable to the signal. Therefore, the higher the noise ceiling, the better the signal quality. The mean and standard deviation of noise ceiling estimated across all voxels in each ROI are V1 (31.06% \pm 24.01%), V2 (29.94% \pm 23.86%), V4 (31.82% \pm 18.78%), LO (29.33% \pm 14.95%), TO (43.043% \pm 20.41%), VO (31.59% \pm 15.55%), PHC (30.04% \pm 17.22%).

Figure S5

a.



b.



a. This table summarizes the replication of our key findings across three additional subjects from the NSD⁸ dataset: Subject-2, Subject-5, and Subject-7. Of the eight subjects included in the NSD, these three were chosen, along with Subject-1, due to their completion of the entire NSD natural image viewing session, providing a more adequate data set for the neural predictor training. We show adversarial robustness improvement (first column), neural predictor efficacy (second column, similar to Fig. 1c in the main text), and noise ceiling estimates for each ROI (third column, similar to Fig. S4). While there is variance in the exact hierarchy order of robustness improvement among the subjects, later areas consistently show more substantial improvements

compared to low-level regions. We note that variability in these results may arise from individual differences as well as data quality, as measured by noise ceiling and neural predictor predictability.

b. In these two scatter plots, we show that the observed hierarchy is unlikely to entirely result from such difference in data quality. We plot model accuracy under adversarial attack against mean noise ceiling (left) and neural predictor predictability (right, measured by Pearson's r). The y-axis corresponds to the average accuracy of each model across three adversarial attack strengths (ϵ : 0.007, 0.009, 0.011), with each data point corresponding to an ROI from one of the four subjects. These visualizations show that while higher data quality generally enhances robustness, the performance in lower-level areas such as V1 and V2 does not exceed that of regions higher in the hierarchy, even with higher noise ceilings. V4 often shows moderate improvement irrespective of noise ceiling variations. On the other hand, the performance of higher-level areas appears more closely tied to data quality, and they tend to achieve higher accuracies than earlier regions overall.

References

1. Krizhevsky, A. Learning multiple layers of features from tiny images. (University of Toronto, 2009).
2. Yang, Z. *et al.* TRS: Transferability Reduced Ensemble via Promoting Gradient Diversity and Model Smoothness. in *Advances in Neural Information Processing Systems* vol. 34 17642–17655 (Curran Associates, Inc., 2021).
3. He, K., Zhang, X., Ren, S. & Sun, J. Deep residual learning for image recognition. in *2016 IEEE Conference on Computer Vision and Pattern Recognition (CVPR)* 770–778 (2016). doi:10.1109/CVPR.2016.90.
4. Loshchilov, I. & Hutter, F. Decoupled weight decay regularization. Preprint at <https://doi.org/10.48550/arXiv.1711.05101> (2019).
5. Rosca, M., Weber, T., Gretton, A. & Mohamed, S. A case for new neural network smoothness constraints. in 21–32 (PMLR, 2020).
6. Madry, A., Makelov, A., Schmidt, L., Tsipras, D. & Vladu, A. Towards deep learning models resistant to adversarial attacks. Preprint at <http://arxiv.org/abs/1706.06083> (2019).
7. Papernot, N., McDaniel, P. & Goodfellow, I. Transferability in machine learning: From phenomena to black-box attacks using adversarial samples. Preprint at <http://arxiv.org/abs/1605.07277> (2016).
8. Allen, E. J. *et al.* A massive 7T fMRI dataset to bridge cognitive neuroscience and artificial intelligence. *Nat. Neurosci.* **25**, 116–126 (2022).